Monthly Notices of the ROYAL ASTRONOMICAL SOCIETY

MNRAS **492,** 1531–1542 (2020) doi:10.1093/mnras/stz3380
Advance Access publication 2019 December 6

NaCo polarimetric observations of Sz 91 transitional disc: a remarkable case of dust filtering

Karina Maucó [1,2]★ Johan Olofsson,[1,2] Hector Canovas,[3] Matthias R. Schreiber,[1,2] Valentin Christiaens,[4] Amelia Bayo [1,2] Alice Zurlo,[5] Claudio Cáceres,[1,6] Christophe Pinte [4] Eva Villaver,[7] Julien H. Girard,[8] Lucas Cieza[5] and Matías Montesinos[1,2,9]

[1]*Núcleo Milenio Formación Planetaria - NPF, Universidad de Valparaíso, Av. Gran Bretaña 1111, Valparaíso, Chile*
[2]*Instituto de Física y Astronomía, Facultad de Ciencias, Universidad de Valparaíso, Av. Gran Bretaña 1111, 5030 Casilla, Valparaíso, Chile*
[3]*European Space Astronomy Centre (ESA/ESAC), Operations Department, Villanueva de la Cañada (Madrid), Spain*
[4]*School of Physics and Astronomy, Monash University, Clayton, VIC 3168, Australia*
[5]*Núcleo de Astronomía, Facultad de Ingeniería y Ciencias, Universidad Diego Portales, Av. Ejercito 441, Santiago, Chile*
[6]*Departamento de Ciencias Fisicas, Facultad de Ciencias Exactas, Universidad Andres Bello, Av. Fernandez Concha 700, Las Condes, Santiago, Chile*
[7]*Departamento de Física Teórica, Universidad Autónoma de Madrid, Cantoblanco, E-28049 Madrid, Spain*
[8]*Space Telescope Science Institute, 3700 San Martin Drive, Baltimore, MD 21218, USA*
[9]*Chinese Academy of Sciences South America Center for Astronomy, National Astronomical Observatories, CAS, Beijing 100012, China*

Accepted 2019 November 28. Received 2019 November 13; in original form 2019 August 7

ABSTRACT

We present polarized light observations of the transitional disc around Sz 91 acquired with VLT/NaCo at H (1.7μm) and K_s (2.2μm) bands. We resolve the disc and detect polarized emission up to ∼0.5 arcsec (∼80 au) along with a central cavity at both bands. We computed a radiative transfer model that accounts for the main characteristics of the polarized observations. We found that the emission is best explained by small, porous grains distributed in a disc with a ∼45 au cavity. Previous ALMA observations have revealed a large sub-mm cavity (∼83 au) and extended gas emission from the innermost (<16 au) regions up to almost 400 au from the star. Dynamical clearing by multiple low-mass planets arises as the most probable mechanism for the origin of Sz 91's peculiar structure. Using new $L^{'}$-band ADI observations, we can rule out companions more massive than $M_{\rm p} \geq 8\,M_{\rm Jup}$ beyond 45 au assuming hot-start models. The disc is clearly asymmetric in polarized light along the minor axis, with the north side brighter than the south side. Differences in position angle between the disc observed at sub-mm wavelengths with ALMA and our NaCo observations were found. This suggests that the disc around Sz 91 could be highly structured. Higher signal-to-noise near-IR and sub-mm observations are needed to confirm the existence of such structures and to improve the current understanding of the origin of transitional discs.

Key words: techniques: polarimetric – protoplanetary discs – stars: individual: Sz 91 – stars: variables: TTauri.

1 INTRODUCTION

One of the main, unresolved questions in planet formation is how the material in the disc grows from (sub-μm) interstellar medium dust to planetesimals. In the past years, there has been a lot of attention on pressure bumps at the edges of cavities because they can efficiently trap relatively large dust grains, and those are regions in the discs where dust growth is expected to take place (e.g. Pinilla et al. 2012a, 2015; van der Marel et al. 2015; Macías et al. 2018). Transitional discs (TD) – discs with sub-mm cavities – are then prime targets to study pressure bumps, dust traps, grain growth, and their connection to planet formation.

One of the mechanisms proposed to explain cavities on discs is the accumulation of large particles into pressure bumps created by planet–disc interactions, halting their radial drift to the central star and driving grain growth (Pinilla et al. 2012a). If the planet producing the cavity is massive enough ($M_{\rm p} > 5M_{\rm Jup}$), small and large particles are going to get trapped at the inner edge of the cavity; if instead a low-mass planet ($M_{\rm p} \sim 1M_{\rm Jup}$) is present, then the small

★ E-mail: karina.mauco@uv.cl

Table 1. Summary of observations.

Date	Band	DIT (s)	NDIT	t_{exp} (s)	<seeing> (arcsec)
2017-03-21	H	15	4	4268[a]	0.76 ± 0.14
2017-03-21	K_s	30	8	8640	0.53 ± 0.08
2017-04-11	L'	0.2	100	1080	0.93 ± 0.11
2017-04-12	L'	0.2	100	2760	0.84 ± 0.10
2017-05-15	L'	0.2	100	2280	1.26 ± 0.18

Notes. The fifth column indicates the total (including the four HWP position angles) exposure time for the H and K_s bands.
[a]We discarded nearly 2/3 of these images due to bad weather.

particles will filtrate into the cavity reaching inner regions (Pinilla et al. 2016a). This mechanism seems to explain the differences in radii observed not only between the gaseous and the dusty disc, but also between dust grains of different sizes (e.g. Dong et al. 2012; de Juan Ovelar et al. 2013; Follette et al. 2013; Garufi et al. 2013; van der Marel et al. 2016, 2018).

Dead zones have also been invoked as an alternative mechanism by which particles accumulate in protoplanetary discs producing ring-like structures. In this case, no planets are needed in order to generate the pressure gradient required for dust grains to get trapped. Instead, low-ionization regions in the disc locally reduce the magnetorotational instability (MRI) which causes the gas flow to significantly decrease, accumulating particles near the boundary of the dead zone (Pinilla et al. 2016b).

High-resolution images of protoplanetary discs at sub-mm wavelengths, like the ones reported in the Disk Substructures at High Angular Resolution Project (DSHARP; Andrews et al. 2018; Birnstiel et al. 2018; Dullemond et al. 2018; Guzmán et al. 2018; Huang et al. 2018a,b; Isella et al. 2018; Kurtovic et al. 2018; Pérez et al. 2018; Zhang et al. 2018), have shown with stunning details the variety of sub-structures present in these young systems. Multiple rings and gaps, spiral arms, azimuthal asymmetries/vortices seem to be common features in planet-hosting discs.

Similar advances have been made at optical/NIR wavelengths due to the polarimetric differential imaging technique (PDI; e.g. Canovas et al. 2011; Tsukagoshi et al. 2014; Benisty et al. 2017; Avenhaus et al. 2018), which uses the polarized light scattered at the disc surface, to obtain linear Stokes parameters of the incoming light, without being contaminated by the stellar contribution which is mostly unpolarized. Since the scattered polarized light will depend on the properties of dust grains (reflectivity, albedo, porosity, composition), polarimetric observations provide a useful tool to estimate grain properties in protoplanetary discs.

High-contrast imaging in the IR is a useful technique to detect the companions that could be responsible for the structures observed in protoplanetary discs (e.g. Absil & Mawet 2010; Bowler 2016). Nowadays, adaptive-optics (AO) assisted observations with the so-called angular differential imaging technique (ADI; Marois et al. 2006) are routinely used to search for these young giant exoplanets. Using this strategy with several AO-equipped instruments has allowed to obtain the first images of a protoplanet in the large cavity of the disc surrounding T-Tauri star PDS 70 (Keppler et al. 2018; Müller et al. 2018; Christiaens et al. 2019).

Sz 91 is an M0 T Tauri Star (TTS), located in the Lupus III molecular cloud (Romero et al. 2012), hosting a TD with the largest mm-dust cavity observed in a low-mass star, and with a significant mass accretion rate ($\dot{M} \sim 10^{-8.8}\,M_\odot\,yr^{-1}$) (Alcalá et al. 2017). ALMA observations have revealed a ring-like concentration of mm-sized particles peaking at ∼95 au, and extended gas emission from less than 16 au up to almost 400 au (Canovas et al. 2015c, 2016; Tsukagoshi et al. 2019). PDI observations taken with the Subaru Telescope by Tsukagoshi et al. (2014) showed a crescent-like emission peaking closer to the star than the ALMA sub-mm data. They suggested that the observed polarized intensity originates at the inner edge of the transition disc.

In this paper, we report new PDI observations of Sz 91 obtained in the NIR (H and K_s bands) and new high-contrast ADI observations in the thermal IR (L' band), both obtained with VLT/NaCo.

2 OBSERVATIONS AND DATA REDUCTION

2.1 *H*- and K_s-band polarimetry

We observed Sz 91 in visitor mode with the NaCo instrument (Lenzen et al. 2003; Rousset et al. 2003) at the VLT/UT 1 on 2017 March 21. The observations were carried out in the polarimetric mode using the broad-band NaCo H and K_s filters ($\lambda_c = 1.66$, 2.18 μm, respectively). In this observing mode, a half-wave plate (HWP) first rotates the polarization plane of the incoming light and then a Wollaston prism splits the light into two orthogonally polarized beams, which are projected on different regions of the detector. The pixel size of the camera was set to 0.027 arcsec pixel^{-1}, the readout mode to `Double RdRstRd` and detector mode to `HighDynamic` ensuring a ∼68 e- readout noise and a ∼110 000 e- linear dynamic range. As Sz 91 is relatively faint and red ($m_{2MASS\ H,\ K_s} = 10.1,\ 9.8$), we used the `N20C80` dichroic that sends 80 per cent of the light to the AO wavefront sensor and 20 per cent to the detector to maximize the throughput of our observations.

The observations were divided in several polarimetric cycles where each cycle contains four data cubes, one per HWP position angle (PA) (at 0°, 22.5°, 45°, and 67.5°, measured on sky east from north). The airmass ranged from 1.0 to 1.5 during the complete sequence, which included observations of the comparison star (GSPC S264-D). We used detector integration times (DITs) of 15 and 30 s for the H- and K_s-band observations, respectively. During the K_s-band observations the seeing was very good and stable with a value of 0.53 arcsec ± 0.08 arcsec. The observing conditions degraded during the H-band observations and the average seeing increased to 0.76 arcsec ± 0.14 arcsec. Standard calibrations including dark and flat fields, as well as observations of a photometric standard star (GSPC S264-D) were provided by the ESO observatory. Our observations are summarized in Table 1.

The two simultaneous, orthogonally polarized images recorded on the detector when the HWP is at 0°(45°) were subtracted to produce the Stokes parameter $Q^+(Q^-)$. Repeating this process for the 22.5°(67.5°) angles produces the Stokes $U^+(U^-)$ images. The total intensity (Stokes I) was computed by adding all the images. We used customized scripts to process the raw data following the imaging polarimetry pipeline described by Canovas et al. (2011). First, each science frame was dark current subtracted and flat-field corrected. Hot and dead pixels were identified with a σ-clipping algorithm and masked out using the average of their surrounding good pixels. The two images recorded in each science frame were aligned with an accuracy of 0.05 pixels as described in Canovas et al. (2011, 2015a). This process was applied to every science frame resulting in a data cube for each Stokes $Q^\pm$, $U^\pm$ parameter. The images were median combined and corrected for instrumental polarization using the double-difference method as described in Canovas et al. (2011) to produce the final Stokes Q and U images.

We then derived the polarization angle ($P = 0.5$ arctan (U/Q)), the polarized intensity ($P_I = \sqrt{Q^2 + U^2}$), and the Q_ϕ and U_ϕ images following the Stokes formalism (see Schmid, Joos & Tschan 2006):

$$Q_\phi = +Q\cos(2\phi) + U\sin(2\phi) \quad (1)$$

$$U_\phi = -Q\sin(2\phi) + U\cos(2\phi), \quad (2)$$

where ϕ is the PA of the image coordinates (x, y) with respect to the star location (x_0 , y_0):

$$\phi = \arctan\frac{x - x_0}{y - y_0} + \theta, \quad (3)$$

with θ as the offset needed to correct for instrumental polarization produced by the angular misalignment of the HWP. This is a convenient coordinate system since, under single scattering assumption, all the emission from a protoplanetary disc should be in the azimuthal direction and be observed as a positive signal in Q_ϕ, whereas emission on U_ϕ can be taken as disc residual noise (Schmid et al. 2006). The central $r < 4$ px are dominated by noise, and therefore this region has been masked out and is not considered for the analysis.

Many of the individual frames were slightly overexposed and have saturated and/or non-linear pixels around the star projected centre. We have median combined a subsample of unsaturated frames to construct a representative point spread function (PSF) for each band. From these PSFs we derive a full width at half-maximum (FWHM) of 0.14 and 0.19 arcsec at K_s and H band, respectively. The narrower FWHM at K_s band is most likely related to a better AO performance, as Sz 91 is slightly brighter towards redder wavelengths and the weather conditions were more stable during the K_s observations. Combining these two PSFs with the zero-points derived from the observations of the standard star, we find that the measured flux is consistent, within an error bar of 0.05 mag, with the published 2MASS photometry. We therefore use the 2MASS photometry to calibrate our observations.

At K_s band the disc is clearly detected, while a preliminary analysis of the H-band data set showed that frame selection had to be applied in order to recover the disc signal. We performed data reductions using different subsets of H-band observations in order to obtain the highest signal-to-noise (S/N) disc image. The H-band results here presented were obtained after processing a subset with total exposure time of 1440 s and average seeing of 0.57 arcsec $\pm$ 0.05 arcsec.

2.2 L'-band imaging

In order to search for (sub)stellar companions, we observed Sz 91 with NaCo at L' band ($\lambda_c = 3.80\mu$m) on 2017 April 11, 2017 April 12, and 2017 May 15. The first two data sets were obtained in average and relatively stable conditions, while the last one was acquired under mediocre and more variable seeing. Since Sz 91 is relatively faint ($m_L \approx 9.7$ mag; Wright et al. 2010), no coronagraph was used. All observations were obtained in pupil-tracking mode. The DIT was set to 0.2s and data were obtained in cube mode with 100 frames per cube (NDIT = 100). With this choice of DIT, neither the background thermal emission nor the star itself saturated on the detector. The star was jittered in the three good quadrants of the detector throughout the observing sequence, to allow for an optimal sky subtraction. We considered the plate scale of NaCo to be 0.0271 arcsec $\pm$ 0.0002 pixel^{-1} in L' band, as per the astrometric calibrations presented in Milli et al. (2017). The details of the observations can be found in Table 1.

We implemented our own pipeline to calibrate the data, which is similar to the one used for the NaCo data presented in Milli et al. (2017). Our pipeline is based on routines of the VORTEX IMAGING PACKAGE (VIP; Gomez Gonzalez et al. 2017),[1] an open-source set of python codes for calibration and post-processing of high-contrast images. Our calibration procedure consists of dark subtraction, flat-fielding, bad pixel correction, sky subtraction, centring of the star, and bad frames rejection. For the centring, we fitted the stellar PSF with a Moffat function, and shifted frames to place the stellar centroid on the central pixel of all images.

Given the relatively short integration of each individual data set, we combined them all in a single data cube. The total parallactic angle rotation achieved in the combined data cube is 111.6°. We then removed frames with the least correlated stellar PSF compared to the median of all PSF images, as measured with the Pearson correlation coefficient. About 10 per cent of all frames were removed on that basis. This trimming ensured a good PSF modelling and subtraction in post-processing. For the latter, we used principal component analysis coupled with ADI (PCA-ADI; Amara & Quanz 2012; Soummer, Pueyo & Larkin 2012) as implemented in VIP. We considered PCA-ADI either in full frames or in frames divided in 2-FWHM wide concentric annuli. In the latter case, a threshold in parallactic angle corresponding to 1 FWHM azimuthal motion is used to build the PCA library for each annulus (see e.g. Absil et al. 2013). This is to minimize self-subtraction of any putative companion.

3 MODELLING AND RESULTS

Fig. 1 shows the observed polarized intensity (left), the Q_ϕ (centre), and U_ϕ (right) images for the K_s (top) and H (bottom) bands. We detect two lobes north and south of the star at both bands which correspond to the major axis of the disc. Fainter emission is also seen on the minor axis at the right side, which has been identified as the front-facing side of the disc closest to us (Tsukagoshi et al. 2014, 2019). The disc shows polarized emission above noise level up to ~0.52 arcsec along the major axis in the Q_ϕ maps. A central cavity is observed at both bands as seen by the substantial emission dips close to the centre. The residual signal observed in the U_ϕ images, especially at K_s band, might be related to multiple scattering events where the linear polarization is not purely azimuthal but have a radial contribution, an effect that is even more pronounced for discs with inclinations $\geq$40° (Canovas et al. 2015b; Pohl et al. 2017).

In this section, we aim to provide a radiative transfer model for Sz 91 which reproduces the main characteristics of the polarized emission observed at H and K_s bands. We first estimate the stellar parameters of the source (model inputs) and then fit a radiative transfer model to the observations.

3.1 Stellar properties: VOSA

We estimated the stellar properties of Sz 91 using the Virtual Observatory (VO), VO-tool VOSA[2] (Virtual Observatory SED Analyzer; Bayo et al. 2008). The observed (stellar) SED of the source is compared to the synthetic photometry obtained using a suit of theoretical models via a χ^2 test. In our case, we considered the BT-Settl-CIFIST and Kurucz models in the analysis. For this, we used a distance to the source of $d = 159.06 \pm 1.63$ pc (*Gaia*

[1] https://github.com/vortex-exoplanet/VIP
[2] http://svo2.cab.inta-csic.es/theory/vosa/

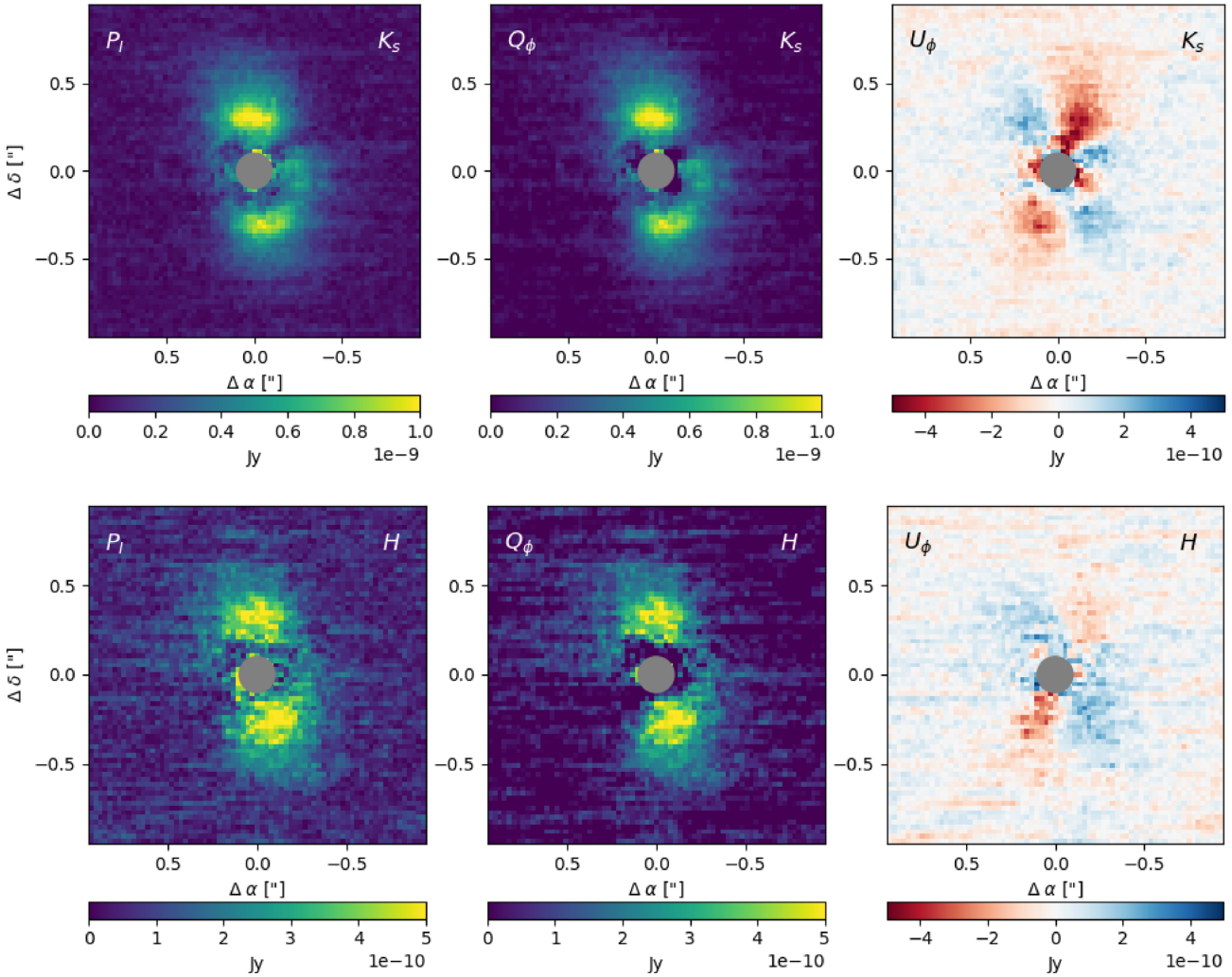

Figure 1. From *left to right*: observed polarized intensity, Q_ϕ, and U_ϕ image at K_s (top) and H (bottom) band. The central 0.1 arcsec region, dominated by noise, has been masked. The observing conditions degraded during the H-band observations. In the U_ϕ images, blue corresponds to positive values, and red to negative values. North is up and east is to the left in all panels.

DR2; Bailer-Jones et al. 2018), and consider the extinction in the line of sight, A_v, also as a fit parameter with an initial upper limit of 2.5 mag taken from the extinction maps of the IRSA Infrared Science Archive (Schlegel, Finkbeiner & Davis 1998).

The best fit was found for the BT-Settl-CIFIST models which are used to infer the total observed flux from the star. We highlight that this estimate is more accurate than the one obtained using a bolometric correction derived only from a single colour. Then, we locate the object in a Hertzsprung–Russell diagram, given its estimated luminosity, L_*, and effective temperature, $T_{\rm eff}$, and use the isochrones and evolutionary tracks from Baraffe et al. (2015) to estimate the stellar mass, M_*, and age of the object. The uncertainties are estimated through a Bayesian approach as explained in Section 3.2.2. The stellar radius, R_*, on the other hand, is estimated using the dilution factor defined as $M_{\rm d} = (R_*/d)^2$, with an uncertainty set by error propagation. Table 2 lists the stellar parameters obtained in this work along with their uncertainties.

The new distance reported in the *Gaia* DR2 catalogue (159 pc; before the source was thought to be located at 200 pc) results in a significantly older age for Sz 91. Using the above methodology, we obtained an age of $5^{+2.4}_{-1.4}$ Myr, older than the ∼3 Myr reported by Tsukagoshi et al. (2019). Since the estimate of ages of individual objects is model dependent and very uncertain, we considered Sz 91 to be older than at least 3 Myr.

Table 2. Stellar parameters.

Parameter	Value	Uncertainty
$T_{\rm eff}$ (K)	3800	[3750, 3850]
Log L_* ($L_\odot$)	−0.59	[−0.63, −0.56]
R_* ($R_\odot$)	1.18	[1.16, 1.18]
M_* ($M_\odot$)	0.58	[0.51, 0.62]
Age (Myr)	5.0	[3.6, 7.4]
A_v (mag)	1.65	[1.58 1.72]

3.2 Radiative transfer modelling

3.2.1 MCFOST model

We used 3D radiative transfer code MCFOST (Pinte, Ménard & Duchêne 2006; Pinte et al. 2009) to model the polarimetric images at H and K_s band. MCFOST computes the dust temperature

Table 3. Model parameters.

Parameter	Value
H_{100} (au)	5
γ	−1
ψ	1.15
R_{out} (au)	150
Parameter space	
R_{in} (au)	35–55, steps = 5
Porosity	0.1–0.9, steps = 0.1
a_{min} (μm)	0.05–0.175, steps = 0.025
δs (μm)	0.05–0.25, steps = 0.05
m_{dust} ($M_\odot$)	10^{-6}–10^{-7}, steps = 1 (in log scale)

Notes. $a_{max} = a_{min} + \delta s$.

structure and scattering source function, under the assumption of radiative equilibrium between the dust and the local radiation field, via a Monte Carlo method. Images are then obtained via a ray-tracing method, which calculates the output intensities by integrating formally the source function estimated by the Monte Carlo calculations. Full calculations of the polarization are included using the Stokes formalism.[3]

The surface density distribution of the disc is described by a simple profile of the form:

$$\Sigma(r) = \Sigma_o \left(\frac{r}{[\mathrm{au}]}\right)^{\gamma}, \quad (4)$$

where Σ_o depends on the mass and size of the disc, and γ represents the power-law index of the surface density profile. A Gaussian profile is used to describe the vertical density distribution with a disc aspect ratio which is radially parametrized as $H(r) = H_{100}(r/100\,\mathrm{au})^{\psi}$, where H_{100} is the scale height at $r = 100$ au, and ψ is the flaring index of the disc. In Table 3 (top), we show the fix model parameters used in this work. We adopted the same H_{100}, γ, and ψ values of Canovas et al. (2015c). The optical depth is changed using different disc's dust masses.

We consider dust grains to be irregular in shape by assuming a distribution of hollow spheres (DHS) as our grain type with a maximum volume void fraction of 0.8 (Min, Hovenier & de Koter 2005). We used an inclination of 49.7° and a PA of 18.1° derived from ALMA observations (Tsukagoshi et al. 2019) assuming that the polarized emission comes from a region co-planar to the sub-mm ring. We stress that there is a small degeneracy between the PA and the grain size (i.e. the phase function), therefore in order to sample in more detail the dust properties (grain size, porosity, dust mass) we fixed the PA of the models to the value estimated from the ALMA observations.

Once the surface density and temperature structure is computed, synthetic ray-traced polarized images (Stokes I, Q, and U maps) can be produced at any wavelength. To compare with our observations, these images were projected into a grid with pixel size of 0.027 arcsec pixel^{-1} (equal to the scale of the NaCo/VLT images). Then, they were scaled using the stellar H and K_s 2MASS magnitudes and were convolved using a Gaussian PSF of 2.5-px width size. Finally, we computed monochromatic Stokes Q_ϕ and U_ϕ images, at 1.7 and 2.2 μm following the same strategy as for the observations (Section 2.1).

[3]http://ipag-old.osug.fr/ pintec/mcfost/docs/html/overview.html

3.2.2 *Best fit*

We ran a grid of 13 500 models varying the following parameters: the minimum/maximum grain size (a_{min}, a_{max}), the grain porosity, the size of the cavity (R_{in}), and the dust mass (m_{dust}). We fixed the outer radius (R_{out}) of the disc to 150 au since it does not affect the final image (it only depends on R_{in}). We considered pure silicate grains with a small amount of carbonaceous particles using the dust opacity from Draine & Lee (1984). Table 3 (bottom) shows the parameter space used in this work.

We determined both the best-fitting model as well as the uncertainties using the Bayesian approach. For this, we constructed the probability distribution functions (PDFs) for our model parameters following a Bayesian analysis as described in Bayo et al. (2008, VOSA 6.0),[4] where for each model we assign a relative probability as

$$W_i = \exp(-\chi_i^2/2), \quad (5)$$

where the subscript i represents each individual model on the grid, and the χ_i^2 represents the goodness of the fit estimated as

$$\chi_i^2 = \sum_n \frac{(Q_\phi^{\mathrm{mod}} - Q_\phi^{\mathrm{obs}})^2}{\sigma^2}, \quad (6)$$

with n the number of pixels included in the fit and σ as the standard deviation measured in concentric annulii from the centre of the U_ϕ^{obs} image excluding the central 0.1 arcsec region. For the χ^2 values, the central $r < 0.15$ arcsec region (dominated by noise) as well as the outer $r > 0.63$ arcsec region (free of disc emission) of each image have been masked out and were not considered for the analysis. Then the probability corresponding to a given parameter value α_j is given by

$$P(\alpha_j) = \sum_i W_i. \quad (7)$$

The final normalized PDF for each parameter is obtained by dividing by the total probability (the sum of the probabilities obtained for each value):

$$P'(\alpha_j) = \frac{\alpha_j}{\sum_i P(\alpha_i)}. \quad (8)$$

Fig. 2 shows the models that best fitted our observations along with their corresponding residuals, which are estimated as $(Q_\phi^{\mathrm{mod}} - Q_\phi^{\mathrm{obs}})/\sigma$. The dashed circles plotted in the left-hand panel circumscribe the area taken into account for the χ^2 fit, basically, all the emission coming from the disc. Table 4 lists the estimated parameters along with their uncertainties, which have been defined as the limits encompassing 68 per cent (1σ) of the total area around the PDF maximum for each parameter. For those cases where the best parameter falls on one of the edges of the range of values used in the models, we have considered these values as upper or lower limits, and they are indicated by parentheses instead of square brackets in Table 4. The PDFs of our model parameters are shown in Fig. 3. As seen in the figure, the polarized emission can be explained by small grains (<0.4 μm), with moderate porosity (<40 per cent), distributed in a ring located at ∼45 au from the central star.

We note, however, that since σ is estimated in concentric rings from the centre, the stronger signal towards the centre of the U_ϕ image will translate into larger uncertainties at the inner regions

[4]http://svo2.cab.inta-csic.es/theory/vosa/index.php

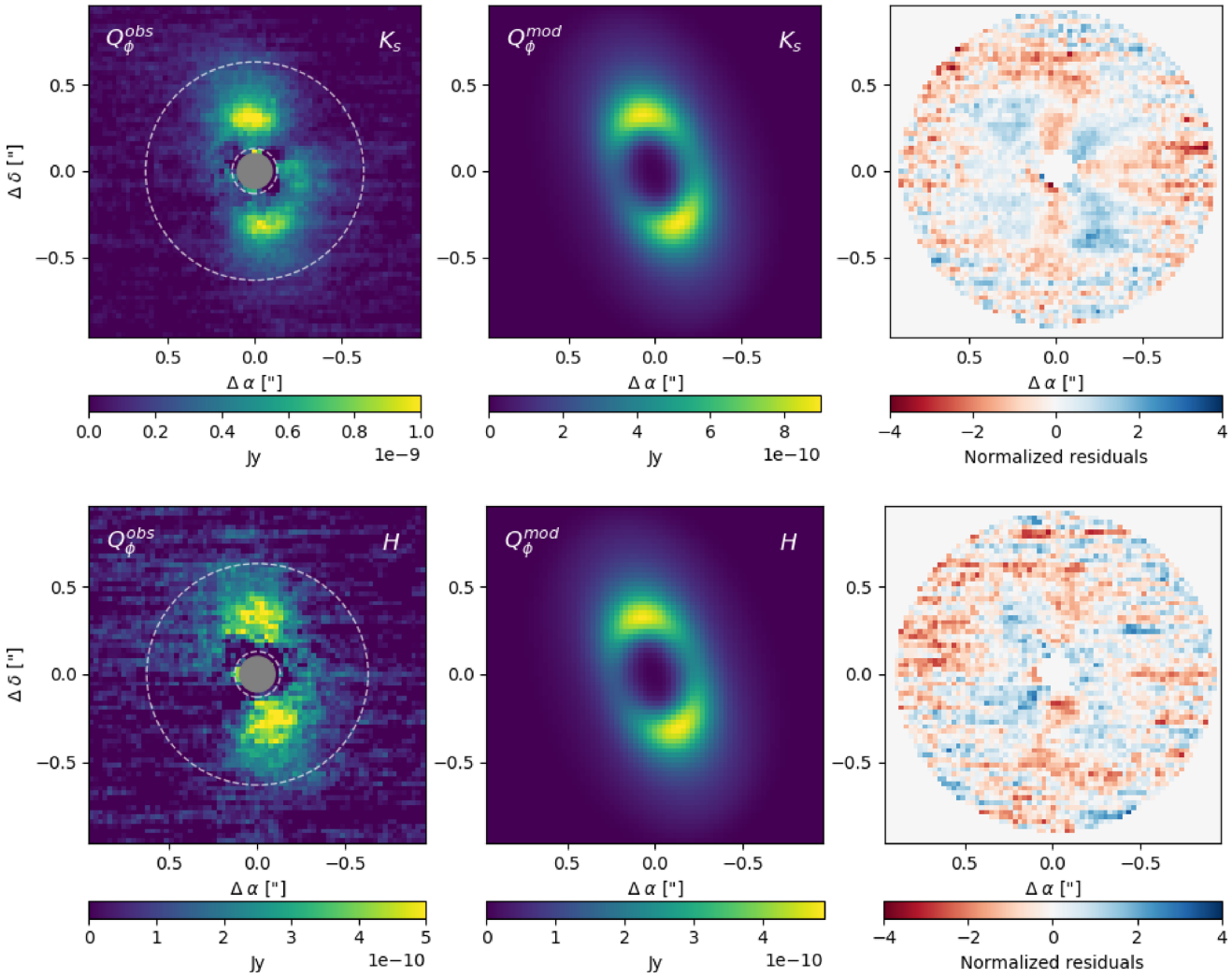

Figure 2. From *left to right*: Q_ϕ observed image, best MCFOST model, normalized residuals for the K_s (top) and H (bottom) bands. The dashed circles plotted in the left-hand panels circumscribe the area taken into account for the χ^2 fit. The faint butterfly pattern observed in the residual map at the K_s band can be the result of the structure of the noise in the U_ϕ image (see the text for details). In the right-hand panels, blue corresponds to positive values, and red to negative values. North is up and east is to the left in all panels.

and hence will give preference to models that best match outer regions. This explains the faint butterfly remnant observed in the residual map at K_s band and why we do not observe any feature on the H band, where the U_ϕ signal is weaker. In any case, we do not see any significant emission on our residual maps besides the noise induced by the faint U_ϕ signal structure, which reinforces the validity of our modelling.

3.2.3 *Caveats of the modelling*

Reproducing the shape of the polarized (or scattered light) phase function is a known challenge when modelling young discs or debris discs (e.g. Milli et al. 2017). As discussed in Min et al. (2016), the polarized phase function may best trace the optical properties of the smallest constituents of dust grains, remaining insensitive to large-scale structures such as aggregates. For this reason, the grain size distribution inferred from our modelling results may be biased towards smaller sizes. As noted above, the models that best explain our NaCo observations are those having a very narrow range of grain sizes (Table 4); similar results were also found for the debris disc around HD 61005 (Olofsson et al. 2016). Grains may well be in the form of aggregates, and the polarized observations would then be dominated by the small monomers (see Section 4.4). Our analysis, based on the observational data currently at hand, suggests that small dust grains are indeed present at the disc surface layers of Sz 91, however, in what shape or form (and as a consequence the exact grain size distribution) remain uncertain. Therefore, both the total dust mass and the optical depth reported here should be treated carefully.

Table 4. Best-fitting values.

Parameter	H	Uncertainty	K	Uncertainty
$R_{\rm in}$ (au)	45	[43, 47]	45	[43, 47]
Porosity	0.40	(<0.40)	0.10	(0.1, 0.17]
$a_{\rm min}$ (μm)	0.15	[0.12, 0.16]	0.15	[0.13, 0.16]
δ_s (μm)	0.05	(0.05, 0.08]	0.20	[0.15, 0.22]
$m_{\rm dust}$ (10^{-7} $M_\odot$)	1.29	[1.07, 1.35]	1.67	[1.59, 2.27]

Notes. Upper/lower limits are indicated by parentheses instead of square brackets.

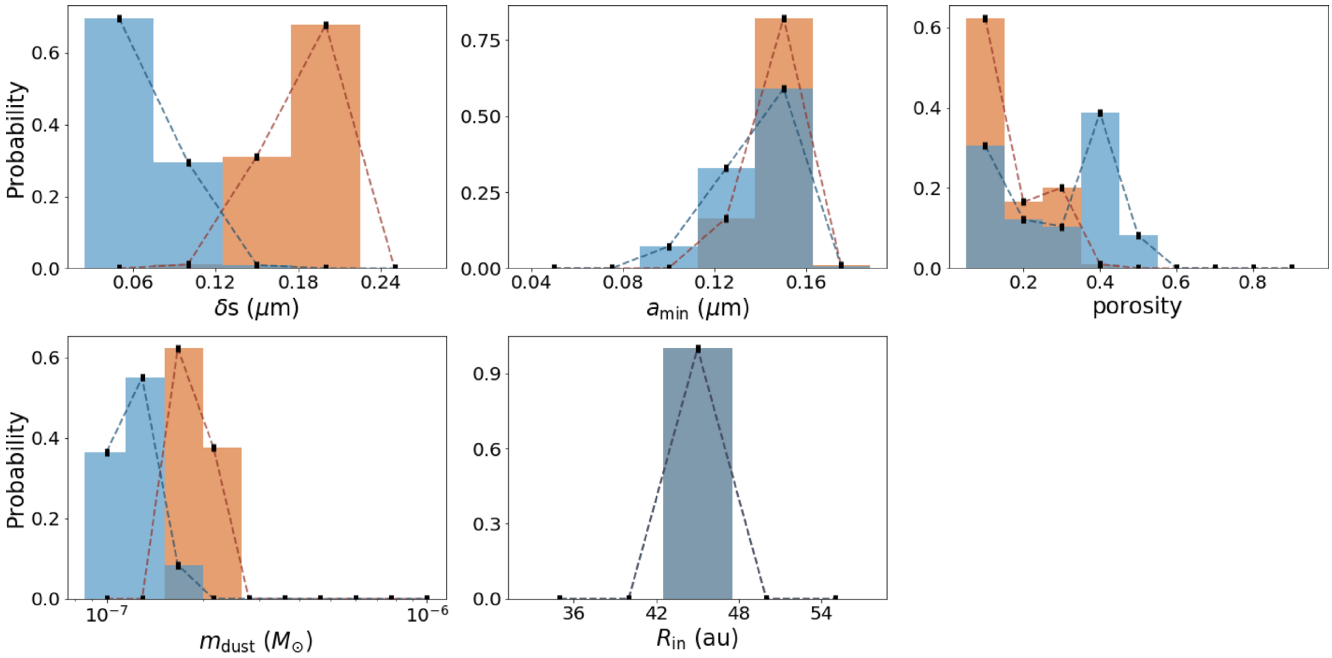

Figure 3. PDFs of our model parameters at K_s (orange) and H (blue) bands. The confidence intervals reported in Table 4 are estimated for a 68 per cent (1σ) confidence level.

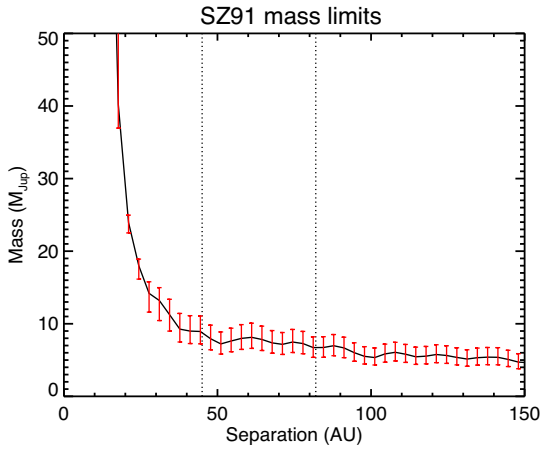

Figure 4. Contrast curve from the NaCo L'-band observations derived using the COND/Dusty models (Allard et al. 2001) for an age of 5 Myr in Jupiter masses (solid line). The error bars indicate the Sz 91 age uncertainty (Table 2). The dotted lines indicate the location of the dust cavities radius observed in polarized light at 45 au (from this work) and in the sub-mm at 82 au (from Tsukagoshi et al. 2019). We can rule out massive giant planets ($\geq$8 M_{Jup}) orbiting beyond 45 au.

3.3 Companion detection limits

Our final L' PCA-ADI images did not reveal any significant point source, for a wide range of tested number of principal components (between 1 and 100). We used VIP (Section 2.2) to compute the 5σ-contrast curve achieved by annular PCA-ADI, using the number of principal components that optimizes contrast at each radial separation.

We then used the COND/Dusty models for brown dwarfs and giant planets atmospheres (Allard et al. 2001) to convert the contrast curve into mass sensitivity limits. We used an age of 5 Myr. Giant planets with masses above $\sim$8 M_{Jup} orbiting beyond 45au could be detected in our observations, as shown in Fig. 4. Note that inside the innermost ($r < 45$ au) regions, massive giant planets can still be present. We remark, however, that the uncertainties are probably very high given the sensitivity of the planet brightness to the initial conditions of planet formation (Mordasini 2013), which in our case are based on 'hot start models', and that the disc emission may mask the planet signal.

4 DISCUSSION

In this section, we inquire about the potential origin of the observed cavity around Sz 91 based on our NaCo data and ALMA observations from previous studies. We also discuss the implications of asymmetric features observed in the polarized emission and in the phase function profile.

4.1 A large cavity in the disc around Sz 91: evidence for dust trapping

ALMA data of Sz 91 have revealed a sub-mm narrow ring at $\sim$95 au from the central star, along with ^{12}CO (3-2) emission extending from the innermost regions ($<$16au) up to almost 400 au (Tsukagoshi et al. 2019). Previous modelling of the ^{12}CO (3-2) emission made by van der Marel et al. (2018) showed a gas-depleted cavity at 39.7 au (after scaling with the new *Gaia* distance) from the star. This apparent inconsistency may be a sensitivity issue since the Tsukagoshi et al. (2019) observations are about twice more sensitive. Additionally, van der Marel et al. (2018) used a simplified model of sharp gas cavity edges, whereas in reality these edges are probably not sharp but rather smooth transitions. This could potentially account for the differences observed by these authors. One should note, however, that even when the gas reaches at least 16 au according to the models of Tsukagoshi et al. (2019), estimated based on blueshifted emission near the highest velocity on the ^{12}CO channel map, their ^{12}CO and HCO^+ moment maps also suggest that there is a lack of signal in the inner regions (rapid decrease of emission towards the star in their figs 4 and 6, although

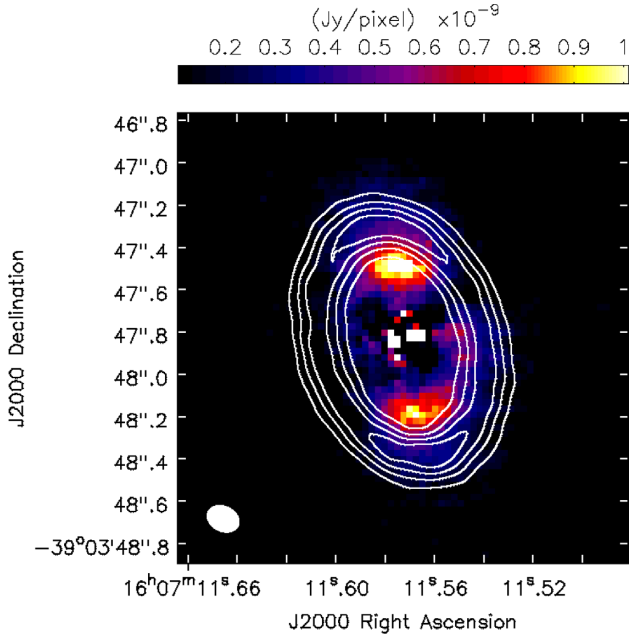

Figure 5. ALMA Band 7 continuum archival image of Sz 91 from project ID 2015.1.01301.S (white contours) overlaid on the K_s band Q_ϕ NaCo image (colour scale). The ALMA synthesized beam is shown as the filled ellipse at the bottom-left corner of the plot. The polarized emission observed with NaCo lies inside the sub-mm cavity.

within one beam of resolution). This could be in line with a drop of density inwards of 40 au (a gas-depleted cavity), as suggested by van der Marel et al. (2018). Nevertheless, this should be treated carefully due to the different angular resolution and sensitivity of these observations.

Polarimetric data, on the other hand, showed a ring-like structure of small (<0.4μm) grains peaking inside the sub-mm cavity as seen in Fig. 5, where we show the ALMA Band 7 continuum archival image of Sz 91 from project ID 2015.1.01301.S (white contours), overlaid on the K_s band Q_ϕ NaCo image (colour scale). TD showing different radii between the gas and dust material, particularly a larger gas extent than (sub)mm dust, have been observed in the past (e.g. Panić et al. 2009; Andrews et al. 2012; Rosenfeld et al. 2013; Canovas et al. 2016; Ansdell et al. 2018; Gabellini et al. 2019).

A few physical mechanisms have been proposed to explain the formation of a large (sub)mm cavity: dynamical clearing by stellar or planetary companions (e.g. Zhu et al. 2011; Pinilla, Benisty & Birnstiel 2012b), an extended dead zone (e.g. Flock et al. 2015; Pinilla et al. 2016b), and internal photoevaporation due to irradiation from the central star (Alexander & Armitage 2007). Models of internal photoevaporation predict dust cavities smaller than ∼20 au and accretion rates of less than 10^{-9} $M_\odot$ yr^{-1} (Owen, Ercolano & Clarke 2011; Ercolano & Pascucci 2017). Therefore, the presence of such a large sub-mm cavity around Sz 91, along with its relatively high mass accretion rate of $\dot{M} \sim 10^{-8.8}$ $M_\odot$ yr^{-1} (Alcalá et al. 2017), make this mechanism very unlikely.

4.1.1 Dynamical clearing by stellar or planetary companions

We have analysed one epoch of high-resolution Las Campanas/MIKE data obtained on 2014 June using the 1.0 arcsec slit. We focus on data from the red arm of MIKE which covers 4900 to 9500 Å with a S/N ∼ 10. The data were reduced using the MIKE pipeline in the Carnegie Observatories' CARPY package (Kelson et al. 2000; Kelson 2003). From this single epoch we can discard an SB2 nature of the object, therefore equal-mass binaries and mass ratios above 0.7 can be discarded out to 1au. Furthermore, Romero et al. (2012) excluded a stellar companion down to separations of ∼30 au and Melo (2003) found no evidence for a close-in binary companion in their 3 yr radial velocity survey down to masses of ≈0.2 $M_\odot$.

This is in agreement with the work of Villenave et al. (2019) where they found that Sz 91's possible companions must be in the planetary mass regime ($M_p < 13 M_{Jup}$), according to the prescription of de Juan Ovelar et al. (2013) which relates the ratio between the radius of the scattered light cavity and that of the sub-mm ring. We remark, however, that using the updated radius for the peak of the sub-mm ring from Tsukagoshi et al. (2019) and that of the scattered light cavity from this work (R_{in} in Table 3), and within the uncertainties, Sz 91 seems to fall in the region of companion masses above 13 M_{Jup} but it is very close to the limit between companion masses above or below this value (red shaded region in fig. 10 of Villenave et al. 2019). According to our new L'-band ADI observations (Section 3.3), on the other hand, we found a mass sensitivity limit for any putative planet of $M_p \leq 8$ M_{Jup} beyond 45 au. Within 35 au, our sensitivity constraints are poor and we cannot rule out the presence of brown dwarf companions (Fig. 4). Follow-up observations are needed in order to completely rule out a stellar companion, however, we will mainly focus on companions of planetary origin hereafter.

In the planet scenario, a large sub-mm cavity is created along with a pressure bump at the outer edge of the cavity. Small dust coupled to the gas move at sub-Keplerian velocities while large particles (>1mm) move with a Keplerian motion. This difference in velocity causes big grains to experience a head wind driven by the gas movement. This makes large particles to loose angular momentum and fall into inner radius. If a positive pressure gradient exists, as a consequence of a planet carving a cavity in the disc, then these particles will get trapped into pressure bumps located at the outer edge of the newly formed cavity.

The fact that the emission from small (μm) grains, as probed by our NaCo observations, peaks inside the sub-mm cavity suggests partial filtration of dust. This could happen in the presence of *low-mass* planets as small grains may not be completely filtered at the outer edge of the planet-induced cavity, and hence pass through the edge to inner regions. Even though Tsukagoshi et al. (2014) suggested that the polarized intensity emission at K_s band was the result of light coming from the inner edge of the disc, it might very well be that this emission is caused by small, optically thin dust passing through the pressure bump into inner regions. Our modelling reveals optical depths around 0.2–0.3, so the polarized emission is rather partially optically thin. In fact, lower optical depths are expected since our models only used small grains. Optically thin dust inside cavities of several TD and pre-transitional discs have been observed (e.g. Calvet et al. 2005; Espaillat et al. 2007, 2010; Follette et al. 2013; Maucó et al. 2018; Pérez-Blanco et al. 2018).

With respect to the gas distribution, if the gas is not depleted inside the sub-mm cavity and embedded planets are indeed the cause of this structure, then these planets must be of low mass (0.1–1 M_{Jup}, Pinilla et al. 2012b; Zhu et al. 2012; Rosotti et al. 2016). This is also consistent in the case of a gas-depleted cavity, as suggested by van der Marel et al. (2018), since multiple low-mass planets can lead to shallower cavities with depletion factors of at least an order of magnitude (Duffell & Dong 2015). Embedded giant planets, on the

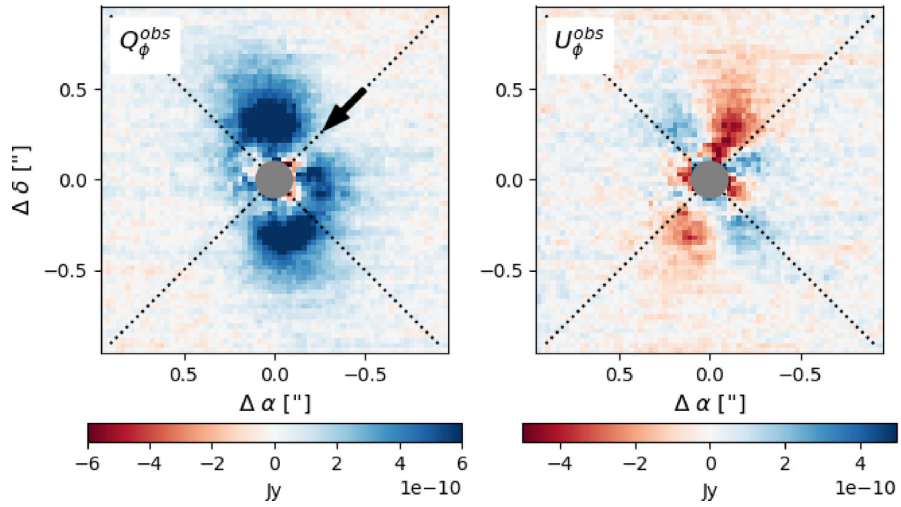

Figure 6. Observed Q_ϕ (left) and U_ϕ (right) images at K_s band. The black arrow indicates the location of the 'dip' in polarized light. The dotted lines have $\pm 45^\circ$ slopes and follow transition regions of positive/negative values in U_ϕ. Note the reddish colours in Q_ϕ which may indicate multiple scattering events (see the text for details).

contrary, have shown to produce deeper cavities in both, the gas and the dust component on protoplanetary discs (e.g. Rice et al. 2006; Pinilla et al. 2016a,b; Gabellini et al. 2019).

4.1.2 An extended dead zone

Dead zones have also been invoked to explain TD structures. These are low-ionization regions on the disc where the high-energy (X-rays and UV) radiation from the star cannot penetrate and, as a consequence, the MRI is suppressed. At the outer edge of these low-ionization regions a bump in the gas density profile is created, due to the change of accretion from the dead to the active MRI zones. Strong accumulation of (sub)mm-sized particles are expected at the location of the outer edge of the dead zone, while the gas is only slightly depleted in the inner part of the disc (e.g. Flock et al. 2015; Pinilla et al. 2016b), as seem to be the case of Sz 91 according to Tsukagoshi et al. (2019). If we considered, on the other hand, a gas-depleted cavity (van der Marel et al. 2018), then it requires the inclusion of a magnetohydrodynamic (MHD) wind to the dead zone in order to create the spatial segregation between the distribution of gas and dust (Pinilla et al. 2016b, 2018). In this case, the gas surface density inside the cavity can be depleted by several orders of magnitude and increases smoothly with radius, in agreement with the ^{12}CO and HCO^+ moment maps of Tsukagoshi et al. (2019). None the less, dead zones always produce a highly depleted gaseous outer disc, which is not the case of Sz 91 (^{12}CO is observed up to $\sim$400 au).

Additionally, Pinilla et al. (2016b) studied the effects of a large dead zone (with an outer edge at $\sim$40 au) in the radial evolution of gas and dust in protoplanetary discs through MHD simulations. On their polarized synthetic images they observed that small (0.65 μm) grains lie just in front of the pressure maximum and slightly closer to the central star than large (mm) grains, although this segregation is very small. In fact, they concluded that this scenario always produces dust cavities at short *and* long wavelengths of similar size at the location of the pressure bump, contrary to what is found in Sz 91 (i.e. μm-sized particles closer in than sub-mm grains).

4.1.3 Final remarks

Overall, Sz 91's morphology suggests that regardless of the origin of the sub-mm cavity, it allows enough gas to reside in the inner regions of the disc. One way to discriminate between these gap-opening mechanisms is to radially resolve the sub-mm ring. Models of embedded planets predict a radially asymmetric ring with a wider outer tail at early times, while dead zones always produce radially symmetric ring-like structures (Pinilla et al. 2018). However, for a $\sim$5 Myr old star it is not clear if this diagnostic still applies. Higher angular resolution observations are needed to validate whether or not low-mass embedded planets are the most likely mechanism for the origin of the cavity in Sz 91.

4.2 Apparent 'dip' on the polarized emission

Fig. 6 shows the observed Q_ϕ (left) and U_ϕ (right) images of Sz 91 at K_s band. For the left-hand panel, we used a different colour bar than that of Fig. 1 in order to better visualize changes on disc emission as well as negative values found close to the centre of the image (reddish colours). The dotted lines have slopes of $\pm 45^\circ$ and, as seen on the right-hand panel, follow transition regions of positive/negative values on the U_ϕ image. The 'dip' observed on the Q_ϕ image located at the NW quadrant, and marked by the black arrow, might be related to one of these transition regions on U_ϕ. In fact, this is the quadrant where the U_ϕ signal is most prominent. We highlight that at these angular positions is where the polarized images are subtracted in order to produce the Stokes parameters (Section 2). Additionally, the negative signal on Q_ϕ supports the fact that multiple scattering events might be contributing to the total emission (Canovas et al. 2015b) at least at the disc inner wall; note that the 'dip' is just located at the same radial location and direction (traced by the dotted line) as the NW negative blob.

All this suggests that the apparent decrease of disc emission in the Q_ϕ image might not be a real dip on the disc, but rather a hint related to the combined effect of the violation of the strictly azimuthal linear polarization assumption (negative values on Q_ϕ) and/or the data reduction process. Besides, the dip is very faint. We quantified how significant the dip is, compared to the region located at the complementary angle in the southern side, by measuring the emission of the disc along azimuthally distributed apertures and found that it is significant by only 1.2σ. Also, it is very close to the central star and might be affected by centring effects. Therefore, the veracity of the 'dip' as a real gap or shadow on the disc is unlikely.

The fact that the same 'dip' also appears at the same location and with the same direction in the Tsukagoshi et al. (2014) observations is certainly intriguing, considering that this data set was taken with a different instrument, at different epochs, and from the Northern hemisphere. None the less, given that Tsukagoshi et al. (2014) also used the same HWP angles to produce their polarized images may suggest that the 'dip' could be the result of the data reduction process and is not of astrophysical origin.

4.3 Polarized phase function

Fig. 7 shows the observed polarized phase function at K_s band of the northern (red) and southern (blue) sides of the disc around Sz 91. To measure the phase function, we placed adjacent circular apertures along an ellipse that traces the main disc (semimajor axis a of 0.34 arcsec, position angle PA of 18.1°, and inclination i of 49.1°, similar to our MCFOST modelling). The size of the aperture was fixed to 0.04 arcsec. For each aperture, we measure the mean flux in the Q_ϕ image, and the 1σ uncertainty corresponds to the standard deviation in the aperture. We normalize both the northern and southern sides by the same factor, so that the northern side phase function has a maximum of 1. We also plot the phase function of the best-fitting model (black line) for comparison. As seen in the figure, the disc is clearly asymmetric along the minor axis, with the northern side being brighter than the southern one (something also visible in Figs 1 and 5). Moreover, the disc also exhibits azimuthal asymmetries, for instance the 'dip' discussed in the above section is clearly seen at low scattering angles (<25°). Our best model represents relatively well both functions, considering that the MCFOST models used here are centro-symmetric, and thus insensitive to any asymmetric feature (a non-symmetric treatment of the polarized emission is out of the scope of this paper).

The intensity peaks for the phase functions of both the north and south sides are separated by less than 23°. We found that this deviation is minimized using a PA of 9° (see Appendix). As stated in Section 3.2.1, we fixed the PA of the models to the value estimated from the ALMA observations (18.1°), since these are the most sensitive data set of Sz 91 to date. None the less, as shown in Fig. 5 there is a shift between the semimajor axis of the sub-mm ring (given by the white concentric ellipse contours) and the intensity peaks (north–south lobs also in contours) in the ALMA image. In fact, the bright lobes seen on ALMA tend to follow more or less the same (azimuthal) position of the NaCo north–south blobs. This peculiar behaviour might explain why a smaller PA produces phase function curves peaking at similar scattering angles at both sides. In any case, the phase function is most sensitive to the properties of the dust (e.g. grain size, porosity) and therefore changes on PA of a few degrees will not affect significantly the results described in Section 3.2.2 and reported in Table 4.

The change in PA between the disc semimajor axis, as measured from the ALMA observations, and the intensity peaks of the polarized emission can be due to: (1) an S/N issue where our observations fail to locate the intensity peaks maximum properly. (2) a projection effect of a flaring disc since ALMA observations probe the disc mid-plane whereas NaCo observations probe the disc surface layers (Stolker et al. 2016). (3) that the disc that we are detecting with our NaCo observations is slightly warped, suggesting a complex and structured circumstellar disc. Our NaCo observations are not sufficient, and higher S/N observations are needed to discriminate between these possible scenarios.

Remarkably, Tsukagoshi et al. (2019) also reported an interesting discrepancy regarding the PA of the gaseous disc, going the other way around. From the first-moment map, the authors estimated a PA of 30° for the gaseous disc, which is 12° off compared to the PA estimated for the dust continuum, and 21° compared to the PA that minimizes the phase functions between the northern and southern sides. None the less, this estimate may not be as constrained as for the dust since it may suffer from cloud contamination or by uncertainties in the position of the central star which in turn affects the location of the minimum/maximum velocity in the first-moment map.

Overall, this suggests that the disc around Sz 91 could be highly structured.

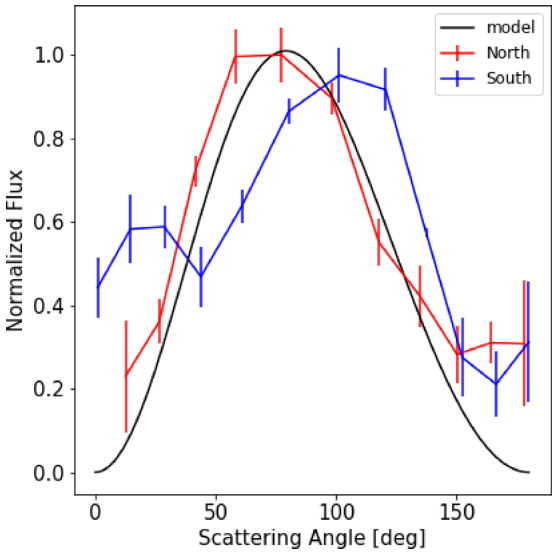

Figure 7. Observed polarized phase function of the northern (red) and southern (blue) sides of Sz 91. We also plot the polarized phase function of the best-fitting model for comparison (black). The disc is clearly asymmetric along the minor axis, being brighter at the north side.

4.4 Impact of dust properties on scatter polarized emission

It is expected that grain growth happens via the sticking of small dust grains together. Therefore, a natural consequence is that grains in protoplanetary discs may resemble aggregates build out of small particles (or 'monomers', see e.g. Min et al. 2016; Roy, Halder & Das 2017; Halder, Deb Roy & Das 2018; Tazaki et al. 2019). Since these aggregates can have different sizes, shapes and with monomers of different compositions, computing realistic optical properties of aggregated particles is a very demanding task. Although exact computations of large aggregates are possible, their use in radiative transfer calculations has been quite limited due to this complexity (Min et al. 2016; Tazaki et al. 2019). This is why approximate methods, like the DHS which simulates irregular shape, porous aggregates for instance, are usually applied in order to significantly decrease the computational demand without losing the essential information of the aggregates optical properties.

Our modelling results suggest that the disc probed with our NaCo observations mostly contains very small grains (<0.4 μm) in order to reproduce the polarized emission at K_s and H bands. The grains must be also relatively porous with porosity values lower than 40 per cent. This implies two possible scenarios: that the emission at the disc surface comes indeed from very small grains, or that large porous aggregates, with radius larger than the wavelength of observation, are present at the upper layers of the disc but the polarized emission we see is dominated by the small monomers

and is insensitive to the global size of the aggregates (one of the conclusions of Min et al. 2016, see Tazaki et al. 2019 as well). Additional observations of the disc at higher S/N ratio, in scattered light (to retrieve the total intensity), and at different wavelengths (e.g. at *J* band, to measure the colour of the disc) may provide new insights in order to discriminate between these possibilities by studying the scattered and/or polarized-light colours and their dependence on size and composition of dust aggregates.

5 CONCLUSIONS

We present polarized light images at K_s and *H* band of the ∼5 Myr protoplanetary disc around the TTS Sz 91 taken with VLT/NaCo. We detect a ring-like structure with bright lobes north and south of the star at both bands. A central cavity is also detected. We provide a radiative transfer model that successfully reproduces the main characteristics of the observed polarized emission, and discuss the implications of this study based on the current observational data available for the source. Our main conclusions are as follows:

(i) The polarized emission is well reproduced using a disc composed of small (<0.4 μm), porous (<40 per cent) grains (adopting a DHS for the scattering theory) with a central cavity of ∼45 au in size. Dust grains are most likely in the form of large aggregates and the polarized observations are probably dominated by the small monomers forming the aggregate.

(ii) Dynamical clearing by multiple low-mass planets arises as the most likely gap-opening mechanism in Sz 91. Although, dead zones may account for the presence of extended gas emission inside the dust cavity up to a few au from the central star, a highly depleted gaseous disc beyond the sub-mm ring is also expected. Furthermore, the cavity size in scattered light is expected to have the same size as the sub-mm cavity, which is not the case of Sz 91. Higher angular resolution observations are needed to confirm the existence of these planets and validate the origin of the disc cavity.

(iii) Our $L^{'}$-band mass detection limits put constraints for possible companions of $M_{\rm p} < 8\ M_{\rm Jup}$ beyond 45au. Within 35au, our sensitivity constraints are poor, and do not rule out the presence of a brown dwarf companion.

(iv) The apparent 'dip' observed in the Q_ϕ image at K_s band is very faint (1.2σ), and it is most likely the result of the data reduction process and/or contamination by multiple scattering events.

(v) The disc is clearly asymmetric along the minor axis with the north side brighter than the south. We also found a change in PA between the disc semimajor axis, measured from the ALMA observations, and the PA needed to minimize the location of the intensity peaks of the phase functions at the north and south sides of our NaCo polarized observations. This suggests that the disc around Sz 91 could be highly structured.

ALMA images with higher resolution and S/N capable of resolving the sub-mm ring in the radial direction as well as non-uniform features in the gas around Sz 91 will undoubtedly help at disentangling between the physical mechanisms behind the origin of the disc cavity. Furthermore, complementary observations in scattered light at different wavelengths using the reference star differential imaging technique, in order to solve the issue of self-subtraction when doing ADI, will also provide new insights about the properties of dust grains at the disc surface layers.

ACKNOWLEDGEMENTS

We thank the anonymous referee for a careful reading of our manuscript and many useful comments. KM acknowledges financial support from CONICYT-FONDECYT project no. 3190859. KM, JO, MRS, AB, CC, MM, and CP acknowledge financial support from the ICM (Iniciativa Científica Milenio) via the Núcleo Milenio de Formación Planetaria grant. JO acknowledges financial support from the Universidad de Valparaíso, and from Fondecyt (grant 1180395). CC acknowledges support from project CONICYT PAI/Concurso Nacional Insercion en la Academia, convocatoria 2015, folio 79150049. MM acknowledges financial support from the Chinese Academy of Sciences (CAS) through a CAS-CONICYT Postdoctoral Fellowship administered by the CAS South America Center for Astronomy (CASSACA) in Santiago, Chile. LC acknowledges financial support from FONDECYT-CONICYT grant no.1171246.

This publication makes use of VOSA, developed under the Spanish Virtual Observatory project supported by the Spanish MINECO through grant AyA2017-84089.

This research has made use of the NASA/IPAC Infrared Science Archive, which is operated by the Jet Propulsion Laboratory, California Institute of Technology, under contract with the National Aeronautics and Space Administration.

This publication makes use of data products from the Two Micron All Sky Survey, which is a joint project of the University of Massachusetts and the Infrared Processing and Analysis Center/California Institute of Technology, funded by the National Aeronautics and Space Administration and the National Science Foundation.

This paper makes use of the following ALMA data: ADS/JAO.ALMA#2015.1.01301.S. ALMA is a partnership of ESO (representing its member states), NSF (USA) and NINS (Japan), together with NRC (Canada), MOST and ASIAA (Taiwan), and KASI (Republic of Korea), in cooperation with the Republic of Chile. The Joint ALMA Observatory is operated by ESO, AUI/NRAO and NAOJ. Based on observations made with ESO Telescopes at the Paranal Observatory under programs ID: 098.C-0420 and 099.C-0336.

Based on observations made with ESO telescopes at the Paranal Observatory under programs ID: 098.C-0420 and 099.C-0336

REFERENCES

Absil O., Mawet D., 2010, A&AR, 18, 317
Absil O. et al., 2013, A&A, 559, L12
Alcalá J. M. et al., 2017, A&A, 600, A20
Alexander R. D., Armitage P. J., 2007, MNRAS, 375, 500
Allard F., Hauschildt P. H., Alexander D. R., Tamanai A., Schweitzer A., 2001, ApJ, 556, 357
Amara A., Quanz S. P., 2012, MNRAS, 427, 948
Andrews S. M. et al., 2012, ApJ, 744, 162
Andrews S. M. et al., 2018, ApJ, 869, L41
Ansdell M. et al., 2018, ApJ, 859, 21
Avenhaus H. et al., 2018, ApJ, 863, 44
Bailer-Jones C. A. L., Rybizki J., Fouesneau M., Mantelet G., Andrae R., 2018, AJ, 156, 58
Baraffe I., Homeier D., Allard F., Chabrier G., 2015, A&A, 577, A42
Bayo A., Rodrigo C., Barrado Y Navascués D., Solano E., Gutiérrez R., Morales-Calderón M., Allard F., 2008, A&A, 492, 277
Benisty M. et al., 2017, A&A, 597, A42
Birnstiel T. et al., 2018, ApJ, 869, L45
Bowler B. P., 2016, PASP, 128, 102001
Calvet N. et al., 2005, ApJ, 630, L185
Canovas H., Rodenhuis M., Jeffers S. V., Min M., Keller C. U., 2011, A&A, 531, A102
Canovas H. et al., 2015a, A&A, 578, L1
Canovas H., Ménard F., de Boer J., Pinte C., Avenhaus H., Schreiber M. R., 2015b, A&A, 582, L7
Canovas H. et al., 2015c, ApJ, 805, 21

Canovas H., Caceres C., Schreiber M. R., Hardy A., Cieza L., Ménard F., Hales A., 2016, MNRAS, 458, L29
Christiaens V. et al., 2019, MNRAS, 486, 5819
de Juan Ovelar M., Min M., Dominik C., Thalmann C., Pinilla P., Benisty M., Birnstiel T., 2013, A&A, 560, A111
Dong R. et al., 2012, ApJ, 750, 161
Draine B. T., Lee H. M., 1984, ApJ, 285, 89
Duffell P. C., Dong R., 2015, ApJ, 802, 42
Dullemond C. P. et al., 2018, ApJ, 869, L46
Ercolano B., Pascucci I., 2017, R. Soc. Open Sci., 4, 170114
Espaillat C., Calvet N., D'Alessio P., Hernández J., Qi C., Hartmann L., Furlan E., Watson D. M., 2007, ApJ, 670, L135
Espaillat C. et al., 2010, ApJ, 717, 441
Flock M., Ruge J. P., Dzyurkevich N., Henning T., Klahr H., Wolf S., 2015, A&A, 574, A68
Follette K. B. et al., 2013, ApJ, 767, 10
Gabellini M. G. U. et al., 2019, MNRAS, 486, 4638
Garufi A. et al., 2013, A&A, 560, A105
Gomez Gonzalez C. A. et al., 2017, AJ, 154, 7
Guzmán V. V. et al., 2018, ApJ, 869, L48
Halder P., Deb Roy P., Das H. S., 2018, Icarus, 312, 45
Huang J. et al., 2018a, ApJ, 869, L42
Huang J. et al., 2018b, ApJ, 869, L43
Isella A. et al., 2018, ApJ, 869, L49
Kelson D. D., 2003, PASP, 115, 688
Kelson D. D., Illingworth G. D., van Dokkum P. G., Franx M., 2000, ApJ, 531, 159
Keppler M. et al., 2018, A&A, 617, A44
Kurtovic N. T. et al., 2018, ApJ, 869, L44
Lenzen R. et al., 2003, in Iye M., Moorwood A. F. M., eds, Proc. SPIE Conf. Ser.Vol. 4841, Instrument Design and Performance for Optical/Infrared Ground-based Telescopes. SPIE, Bellingham, p. 944
Macías E. et al., 2018, ApJ, 865, 37
Marois C., Lafrenière D., Doyon R., Macintosh B., Nadeau D., 2006, ApJ, 641, 556
Maucó K. et al., 2018, ApJ, 859, 1
Melo C. H. F., 2003, A&A, 410, 26
Milli J. et al., 2017, A&A, 597, L2
Min M., Hovenier J. W., de Koter A., 2005, A&A, 432, 909
Min M., Rab C., Woitke P., Dominik C., Ménard F., 2016, A&A, 585, A13
Mordasini C., 2013, A&A, 558, A113
Müller A. et al., 2018, A&A, 617, L2
Olofsson J. et al., 2016, A&A, 591, A108
Owen J. E., Ercolano B., Clarke C. J., 2011, MNRAS, 412, 13
Panić O., Hogerheijde M. R., Wilner D., Qi C., 2009, A&A, 501, 269
Pérez-Blanco A. et al., 2018, ApJ, 867, 116
Pérez L. M. et al., 2018, ApJ, 869, L50
Pinilla P., Birnstiel T., Ricci L., Dullemond C. P., Uribe A. L., Testi L., Natta A., 2012a, A&A, 538, A114
Pinilla P., Benisty M., Birnstiel T., 2012b, A&A, 545, A81
Pinilla P. et al., 2015, A&A, 584, A16
Pinilla P., Klarmann L., Birnstiel T., Benisty M., Dominik C., Dullemond C. P., 2016a, A&A, 585, A35
Pinilla P., Flock M., Ovelar M. d. J., Birnstiel T., 2016b, A&A, 596, A81
Pinilla P. et al., 2018, ApJ, 859, 32
Pinte C., Ménard F., Duchêne G., 2006, in Stee P., ed., EAS Publ. Ser.Vol. 18, Radiative Transfer in Protoplanetary Disks. Cambridge Univ. Press, Cambridge, p. 157
Pinte C., Harries T. J., Min M., Watson A. M., Dullemond C. P., Woitke P., Ménard F., Durán-Rojas M. C., 2009, A&A, 498, 967
Pohl A. et al., 2017, A&A, 605, A34
Rice W. K. M., Armitage P. J., Wood K., Lodato G., 2006, MNRAS, 373, 1619
Romero G. A., Schreiber M. R., Cieza L. A., Rebassa-Mansergas A., Merín B., Smith Castelli A. V., Allen L. E., Morrell N., 2012, ApJ, 749, 79
Rosenfeld K. A., Andrews S. M., Wilner D. J., Kastner J. H., McClure M. K., 2013, ApJ, 775, 136
Rosotti G. P., Juhasz A., Booth R. A., Clarke C. J., 2016, MNRAS, 459, 2790
Rousset G. et al., 2003, in Wizinowich P. L., Bonaccini D., eds, Proc. SPIE Conf. Ser.Vol. 4882, Adaptive Optical System Technologies II. SPIE, Bellingham, p. 140
Roy P. D., Halder P., Das H. S., 2017, Astrophys Space Sci, 362
Schlegel D. J., Finkbeiner D. P., Davis M., 1998, ApJ, 500, 525
Schmid H. M., Joos F., Tschan D., 2006, A&A, 452, 657
Soummer R., Pueyo L., Larkin J., 2012, ApJ, 755, L28
Stolker T. et al., 2016, A&A, 595, A113
Tazaki R., Tanaka H., Muto T., Kataoka A., Okuzumi S., 2019, MNRAS, 485, 4951
Tsukagoshi T. et al., 2014, ApJ, 783, 90
Tsukagoshi T. et al., 2019, ApJ, 871, 5
van der Marel N., Pinilla P., Tobin J., van Kempen T., Andrews S., Ricci L., Birnstiel T., 2015, ApJ, 810, L7
van der Marel N., van Dishoeck E. F., Bruderer S., Andrews S. M., Pontoppidan K. M., Herczeg G. J., van Kempen T., Miotello A., 2016, A&A, 585, A58
van der Marel N. et al., 2018, ApJ, 854, 177
Villenave M. et al., 2019, A&A, 624, A7
Wright E. L. et al., 2010, AJ, 140, 1868
Zhang S. et al., 2018, ApJ, 869, L47
Zhu Z., Hartmann L., Nelson R. P., Gammie C. F., 2011, ApJ, 746, 110
Zhu Z., Nelson R. P., Dong R., Espaillat C., Hartmann L., 2012, ApJ, 755, 6

APPENDIX A: POLARIZED PHASE FUNCTION FOR A DIFFERENT PA

In order to find the PA that minimizes the phase functions between the northern and southern sides of the disc around Sz 91 shown in Fig. 7, we estimated both phase functions using a range of PA (from 6° to 20°) and compared the difference between the intensity peaks of both sides in each case. We found that for a PA of 9° this difference is minimized.

Fig. A1 shows the polarized phase function of the NaCo K_s observations of the northern (red) and southern (blue) sides of the disc around Sz 91 using a PA = 9°.

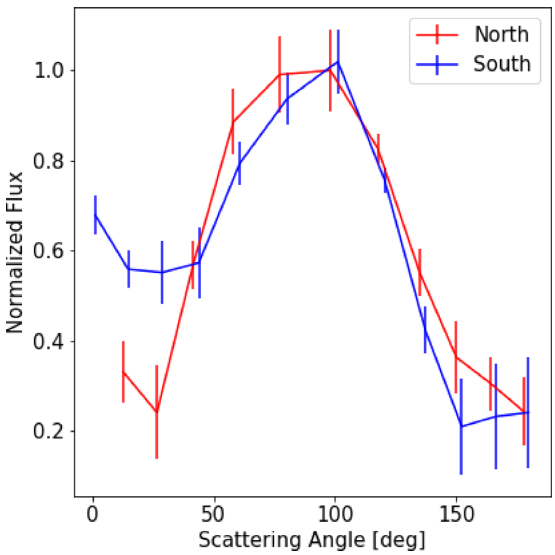

Figure A1. Polarized phase function of the NaCo K_s observations of the northern (red) and southern (blue) sides of the disc around Sz 91 using a PA = 9°.

This paper has been typeset from a TEX/LATEX file prepared by the author.